UNIVERSITY OF
OXFORD

OCCAM
OXFORD CENTRE FOR COLLABORATIVE APPLIED MATHEMATICS

Microfluidic Immunomagnetic Multi-Target Sorting A Model for Controlling Deflection of Paramagnetic Beads

by

Scott S.H. Tsai
Ian M. Griffiths
Howard A. Stone

OCCAM Preprint Number 12/101

Journal Name

Dynamic Article Links ►

Cite this: DOI: 10.1039/c0xx00000x

www.rsc.org/xxxxxx

ARTICLE TYPE

Microfluidic Immunomagnetic Multi-Target Sorting – A Model for Controlling Deflection of Paramagnetic Beads

Scott S.H. Tsai,[a] Ian M. Griffiths[b] and Howard A. Stone[c]

Received (in XXX, XXX) Xth XXXXXXXXX 20XX, Accepted Xth XXXXXXXXX 20XX

DOI: 10.1039/b000000x

We describe a microfluidic system that uses a magnetic field to sort paramagnetic beads by deflecting them in the direction normal to the flow. Our experiments systematically study the dependence of the beads' deflection on: bead size and susceptibility, magnet strength, fluid speed and viscosity, and device geometry. We also develop a design parameter that can aid in the design of microfluidic devices for immunomagnetic multi-target sorting.

Introduction

Immunomagnetic separation uses biochemically functionalized paramagnetic beads that bind specifically to targets to produce separation from a solution by applying a magnetic field.[1] The targets are cells, proteins[2-3] and other biological components. Microfluidic immunomagnetic collection of a single target from a solution of many targets has been studied extensively and applied to biomedical processes such as capturing specific cells,[4-5] cleansing blood of pathogens,[6] and the detection of diseases such as cancer.[7-8] In these applications, the targets and magnetic beads flow through a microchannel, where an applied magnetic field produces a force that causes the beads and their cargo either to migrate to another streamline or to become captured. Theoretical models of bead trajectories and capture efficiencies have also been developed.[9-17] To date, these models and experiments demonstrate that microfluidic immunomagnetic systems can collect a single target from a solution of many targets.

Pamme et al.[18-19] experimentally demonstrated that microfluidic magnetic systems can potentially sort multiple targets. Paramagnetic beads of different radii and susceptibilities flowed through a microchannel with an applied magnetic field and exited through different outlets. Similar designs with an expanded number of outlets[20] and different magnet configurations[21-23] were demonstrated more recently. It has also been shown that when distinct solutions of different cell types are incubated with paramagnetic beads for different amounts of time, then upon mixing the different solutions and flowing them through a microchannel with an applied magnetic field, the different cells can be separated.[24]

These examples illustrate that microfluidic immunomagnetic systems have the potential to continuously sort multiple targets in a parallel fashion. However, until now, there has been little insight from the standpoint of modeling of the physics involved in controlling the sorting of different beads and targets. In our work, we identify variables that control the deflection that beads with different properties experience in a continuous-flow microfluidic magnetic multi-target sorter. We analytically derive and experimentally test a dimensionless design parameter that allows a designer to choose paramagnetic beads, permanent magnets, pumping velocities, and channel geometries based on how many targets there are and where they exit the channel. Our results are in good agreement with other experimental results in the literature.

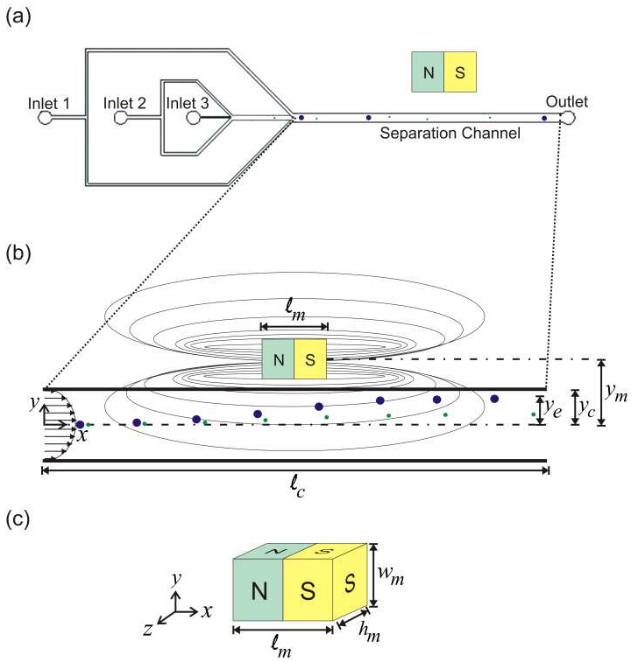

Figure 1 (a) Schematic design of a microfluidic multi-target sorter. Inlets 1 and 2 are flow-focusing fluid inlets. A suspension of beads flows through inlet 3. The beads flow through (b) the separation channel, passing permanent magnet(s). Approximate magnetic field lines are indicated. Multi-target sorting relies on the fact that different types of paramagnetic beads exit at different distances, y_e, away from the channel centerline. To illustrate the multi-target sorting, we have shown trajectories of two different beads. (c) The dimensions of the magnet. (Color on-line)

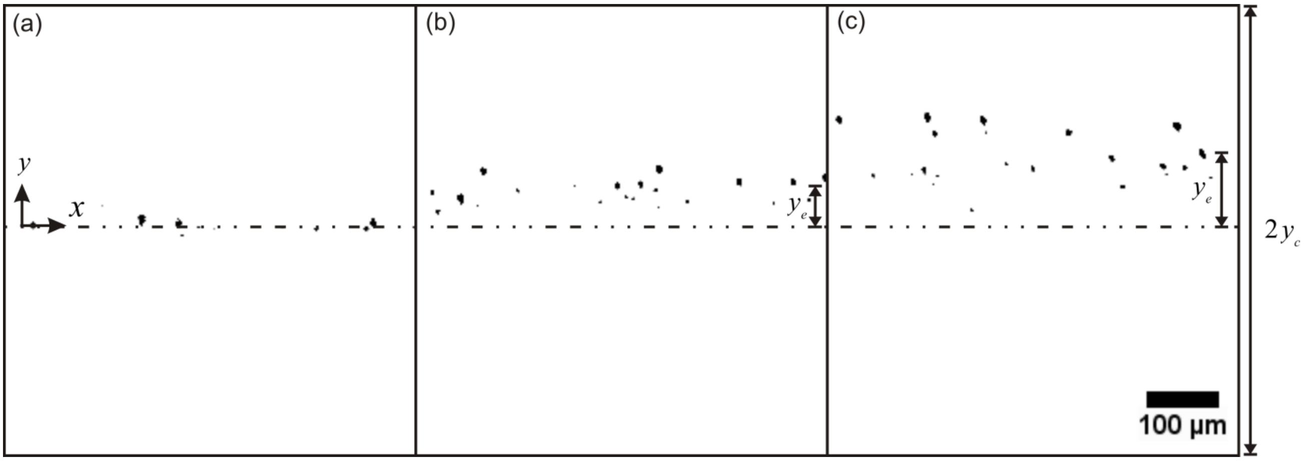

Figure 2 Frames taken from high-speed videos near the end of the separation channel. (a) Control experiment with no magnetic field; 1.4 µm radius beads are focused to the center of the channel and flow horizontally at approximately 10 cm s^{-1}. The same beads, flowing at (b) 2 cm s^{-1} and (c) 1 cm s^{-1} are deflected from the centerline when a magnetic field is applied. The flow is from left to right, and y_e is measured from the centerline at the end of the channel. Beads out of focus appear larger.

Experimental

A schematic diagram of the microfluidic device that we fabricated and tested is shown in Figure 1(a). Polydimethylsiloxane (PDMS, Sylgard 184 silicone elastomer kit, Dow Corning, Midland, MI, USA) layers are made using standard soft-lithography techniques.[25] A 1.5 mm thick PDMS layer containing the channel patterns is bonded to a 1.5 mm thick patternless PDMS layer, which encloses the channels. A rectangular slot is cut adjacent to the separation channel for placement of the magnets. The two 1.5 mm thick PDMS layers are bonded together with the channels enclosed in the middle so that the permanent magnet is situated adjacent to the separation channel, with the channel at approximately the midpoint between the top and bottom of the magnet. This minimizes the vertical component of the magnetic forces on the beads. A glass microscope slide (Dow Corning, Midland, MI, USA) is then bonded to the patternless PDMS layer by plasma treatment. The channels are all 50 µm in height, and the separation channel is 615 µm in width and 20 mm in length.

The device has three inlets and one outlet (see Figure 1(a)); fluid is pumped at a constant flow rate (Harvard Apparatus, Holliston, MA, USA) through the outer two inlets and a suspension of beads, at a bead number density of 3 x 10^7 beads mL^{-1}, is pumped through the inner inlet. We vary the average fluid speed in the separation channel u_o, in our experiments from 1 - 15 cm s^{-1}. A hydrodynamic-focusing[26] configuration has been adopted since a straight line of beads entering the separation channel will result in the best possible control of the exit position. A Phantom V9 (Vision Research, Wayne, NJ, USA) video camera recording at 3000 fps is used in combination with bright-field microscopy (Leica Microsystems, Wetzlar, Germany) to capture the motion of the paramagnetic beads.

Paramagnetic beads (Life Technologies, Carlsbad, CA USA) made with a polystyrene matrix embedded with Fe_2O_3 nanoparticles are suspended in deionized water (density, ρ = 10^3 kg m^{-3}, and dynamic viscosity, η = 10^{-3} kg m^{-1} s^{-1}) and flow through the microfluidic device. The bead radii a = 0.5 and 1.4 µm. We do not initially know the value of the susceptibility, χ, but we assume that they are constant for each bead size and we calculate χ later by comparing with our model.

Applied magnetic fields, $\boldsymbol{H}$ (A m^{-1}), are supplied by permanent magnets. We use $Nd_2Fe_{14}B$ magnets (KJ Magnetics, Jamison, PA, USA) having a magnetization M = 10^6 A m^{-1}. The magnets are cubes of 3.175 mm side length. We change the length of the magnet-stack, ℓ_m, in our system from 6.4 to 9.5 mm by stacking two or three magnets together. The magnets are always aligned from pole to pole.

Figure 1(b) is a schematic diagram of the separation channel of the microfluidic sorting device. The geometrical variables we vary are: the length of the stack of magnets, ℓ_m, and the distance from the centerline to the center of the magnet, y_m. The length of the separation channel, ℓ_c, and the distance from the centerline to the channel wall, y_c, are both held constant in our experiments. We measure the exit position of the beads, y_e, with respect to the y-axis. Table 1 is a summary of the variables and their ranges in our experiments.

Variable	y_m (mm)	u_o (cm s^{-1})	ℓ_m (mm)	a (µm)	χ
Baseline	3	10	6.4	0.5	2.5 x 10^{-2}
Range	3 – 4.5	1 – 15	6.4 – 9.5	0.5 – 1.4	2.0 – 2.5 x 10^{-2}

Table 1 Baseline and ranges of values used in the experiments. The values for y_m, ℓ_m, a, and χ alter between the extreme values indicated in the table; u_o varies between 1 and 15 cm s^{-1} in a step-wise manner. The values of χ were determined by comparing with our model.

Results and discussion

Experimental results

The images in Figure 2 are representative frames taken from high-speed videos of the experiments. Here, 1.4 µm radius beads are initially focused to the center of the separation channel. The beads flow from left to right, passing the permanent magnet(s) placed adjacent to the channel. The average deflections of the paramagnetic beads right before exiting the outlet, $\overline{y}_e$, are measured relative to the exit positions of the beads in control experiments (with no applied magnetic field): $\overline{y}_e = \overline{y}_e\left(H\right) - \overline{y}_e\left(H=0\right)$. As we would expect, due to the flow focusing, $\overline{y}_e\left(H=0\right) \approx 0$. The spread in deflections measured about this mean was $\leq$ 8 µm. The average deflections of the beads are recorded each time as we decrease the average fluid speed, u_o, from 15 to 1 cm s^{-1}. As the fluid speed is decreased, the beads exit closer to the channel wall, away from the centerline.

The large distributions of exit positions for the beads in cases where the magnetic field is applied and when the flow speed is low (Fig. 2) highlight the need to focus the beads at the channel inlet. Without focusing, the distribution of beads at the exit would be even larger.

The average deflections of the beads are plotted versus the average fluid speeds in Figure 3. Here, the baseline data points are obtained with 0.5 µm radius beads, with $y_m \approx$ 3 mm and $\ell_m \approx$ 6.4 mm. Subsequent data points are results from changing a, χ, y_m, and/or ℓ_m according to the values in Table 1. Generally, as the speed of the fluid is increased, the residence time of the beads in the applied magnetic field decreases. Since the magnetic force on the beads is the same regardless of the fluid speed, the beads will deflect less as the fluid speed is increased.

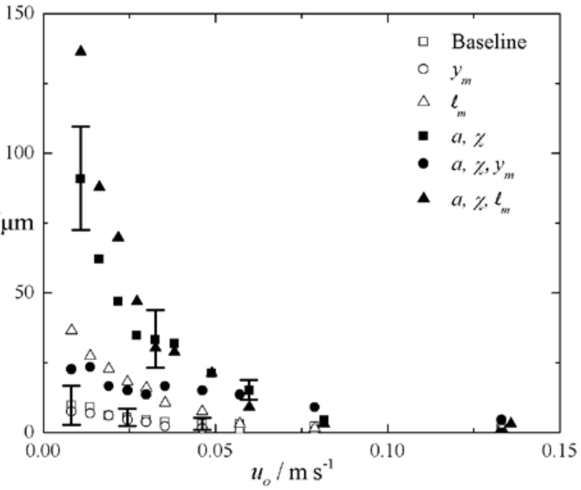

Figure 3 The exit position of the beads, $\bar{y}_e$ is plotted against the average fluid velocity, u_o. The plot shows that the exit position is determined by a competition between magnetic and viscous forces. As the bead size is decreased, the magnetic strength decreases and the beads exit at a position closer to the centerline. Conversely, as fluid speed is reduced, the drag force is decreased, and the beads exit at a distance farther from the centerline. Error bars indicate the distribution of bead exit positions. The legend denotes the variables we have changed according to the ranges shown in Table 1: bead radius (a) and susceptibility (χ), average fluid speed (u_o), the length of the magnets (ℓ_m) and the distance between the magnet and the channel (y_m).

The experimental results show that the 1.4 µm radius beads, for the most part, have larger deflections than the smaller 0.5 µm radius beads, which indicates that larger beads experience a stronger magnetic force. Increasing ℓ_m from 6.4 to 9.5 mm increases the magnetic moment of the magnet, $m = \ell_m w_m h_m M$, increasing the force on the bead and the deflection. Changing y_m from 3 to 4.5 mm dramatically reduces the deflection of the beads.

Scaling analysis

The Reynolds number of the beads during flow in our experiments is given by $Re_b = \rho a\left(\dot{\gamma} a\right)/\eta$. Here, $\dot{\gamma} = u_o/h$ is a typical shear rate experienced by the beads, and h = 50 µm, so $Re_b = \left(\rho u_o h/\eta\right)\left(a/h\right)^2 \quad O\left(10^{-2}\right)$ for our experiments, and so we may safely neglect inertial forces in our model.

The Stokes-Einstein equation predicts the diffusion coefficient of the beads, D (m^2 s^{-1}), due to thermal fluctuations. In our setup, $D = k_BT/6\pi\eta a = O(10^{-12})$ m^2 s^{-1}, where k_B is Boltzmann's constant (1.38 × 10^{-23} m^2 kg s^{-2} K^{-1}) and T (293 K) is temperature. The characteristic length a bead moves due to thermal fluctuations, while it is in the separation channel, is $(D\ell_m/u_o)^{1/2} = O(10^{-1})$ µm << $\bar{y}_e$, which allows us to neglect the effects of thermal fluctuations. We also choose to neglect bead-bead hydrodynamic interactions based on the assumption that we begin with a dilute suspension of beads. (The effects of bead-bead hydrodynamic interactions in high bead density microfluidic immunomagnetic systems have been discussed in the work of Mikkelsen *et al.*[10]) The dominant forces on the beads are Stokes drag, ($\boldsymbol{F_d}$) and magnetic force, ($\boldsymbol{F_m}$). Thus,

$$\boldsymbol{F_d} + \boldsymbol{F_m} = \boldsymbol{0}. \tag{1}$$

Stokes drag, $\boldsymbol{F_d} = -6\pi\eta a(\boldsymbol{v} - \boldsymbol{u})$, occurs due to the relative movement of a bead to the fluid. The force on a spherical paramagnetic bead in an external magnetic field[9-11, 14] is $\boldsymbol{F_m} = 4\pi a^3\mu_o(\chi/(\chi+3))\nabla H^2$. Here, $\boldsymbol{v}$ is the velocity of the bead (m s^{-1}), $\boldsymbol{u}$ is the velocity of the fluid (m s^{-1}), μ_o is the permeability of free space (1.257 x 10^{-6} m kg s^{-2} A^{-2}), and $\boldsymbol{H}$ is the external magnetic field (A m^{-1}). The drag on the bead is proportional to the bead radius and the velocity difference between the bead and the surrounding fluid. The magnetic force is proportional to the volume of the bead, its magnetic susceptibility, and the gradient of the square of the magnetic field.

Rearranging equation (1) gives us the velocity of the bead,

$$\boldsymbol{v} =+ \frac{2}{3}\frac{\mu_o a^2}{\eta}\frac{\chi}{\chi+3}\nabla H^2 \quad \boldsymbol{u}. \tag{2}$$

The magnetic field scales as $H \approx \left(\ell_m w_m h_m M\right)/\left(y_m - y\right)^3$. The derivative of H^2 with respect to y, scales as $\frac{dH^2}{dy} \approx \left(\ell_m^2 w_m^2 h_m^2 M^2\right)/\left(y_m - y\right)^7$. However, microfluidic channels used for immunomagnetic sorting are typically O(100 µm) in width (the largest possible value of $\bar{y}_e$) and the length of the permanent magnets used, y_m, are usually O(1 mm), so we can make the reasonable assumption, $\frac{dH^2}{dy} \approx \left(\ell_m^2 w_m^2 h_m^2 M^2\right)/\left(y_m\right)^7$. Since y_e is dependent on the time the bead is exposed to the magnetic field, we approximate a characteristic residence time for flow in the channel as $\Delta t \approx \ell_m/u_o$. Thus, dividing the y-component of equation (2) by y_c gives us a prediction of the dimensionless exit position, $y_e' = \bar{y}_e/y_c$, based on a dimensionless design parameter, Ω:

$$y_e' = \frac{\bar{y}_e}{y_c} = \kappa\Omega, \tag{3a}$$

where $$\Omega = \frac{\chi}{\chi+3}\frac{\mu_o a^2 \ell_m^3 w_m^2 h_m^2 M^2}{y_c \eta u_o y_m^7}, \tag{3b}$$

and κ is a dimensionless scaling constant.

Equation (3), which is derived from a balance of magnetic and fluid forces, agrees qualitatively with what is observed experimentally. The result shows that when the magnetic force increases, the beads exit farther from the centerline. On the other hand, when the fluid velocity and viscosity terms increase, the magnetic beads exit close to the centerline. Our scaling analysis reveals a linear dependence between the exit position, y'_e, and the design parameter, Ω. The scaling analysis reveals several important geometrical variables as well. The exit position of the beads depends significantly on how far the magnet is from the centerline, y_m. The length of the magnet stack, ℓ_m, is also an important geometrical scale because it determines how long the magnetic force is exerted on the beads.

In the literature, several theoretical papers[9, 14-15] that study capture efficiencies of microfluidic magnetic devices also develop dimensionless parameters from a balance of magnetic and fluid drag forces. Sinha *et al.*,[9] through dimensional reasoning, identify a parameter that characterizes the critical magnetic bead entrance position at which eventual bead capture takes place before the channel exit. Their parameter is equivalent to Ω, albeit modified by the inverse aspect ratio y_c/ℓ_m, which reinforces our more detailed scaling-law argument. We note that, although they assume a point-dipole magnet for their setup, they measure the critical bead entrance position for complete bead-capture, y_{ent}, and obtain an experimental power-law, $y_{ent} \propto \Omega^{0.87}$, for small values of Ω, which is close to our scaling prediction, $y'_e \propto \Omega$.

Detailed calculations

In a detailed calculation to obtain a value for the coefficient κ, we choose the origin of our coordinate system to lie at the center of the entrance of the channel as depicted in Figure 1(b) and non-dimensionalize the system via

$$(x, y, z) = \ell_m (x', y', z'), \; t = \frac{\ell_m}{u_o} t', \; \boldsymbol{H} = \frac{M}{4\pi} \boldsymbol{H}', \tag{4}$$

The dimensionless magnetic field, $\boldsymbol{H}'$, at a position (x', y', z') may be determined analytically for a three-dimensional rectangular magnet of dimensions of ℓ_m x w_m x h_m and magnetized in the x-direction (as shown in Figure 1(c)) in terms of the dimensionless parameters

$$L_c = \frac{\ell_c}{\ell_m}, \; H_m = \frac{h_m}{\ell_m}, \; W_m = \frac{w_m}{\ell_m}, \quad Y_m = \frac{y_m}{\ell_m}, \; Y_c = \frac{y_c}{\ell_m}, \tag{5}$$

which characterize the geometrical properties of the magnet and channel. (See Appendix for calculation.)

We denote the dimensionless position of the bead in the channel by $(x', y', z') = (x'_b(t'), Y_c y'_b(t'), z'_b(t'))$, where the different scaling for y_b reflects the fact that deflections in the y-direction occur on the scale of the channel width, y_c. The dimensionless version of equation (2) is then

$$\frac{dx'_b}{dt'} = 1 + Y_c \beta \Omega \frac{\partial H'^2}{\partial x'}\bigg|_{(x',y',z')=(x'_b, Y_c y'_b, z'_b)}, \tag{6a}$$

$$\frac{dy'_b}{dt'} = \beta \Omega \frac{\partial H'^2}{\partial y'}\bigg|_{(x',y',z')=(x'_b, Y_c y'_b, z'_b)}, \tag{6b}$$

$$\frac{dz'_b}{dt'} = Y_c \beta \Omega \frac{\partial H'^2}{\partial z'}\bigg|_{(x',y',z')=(x'_b, Y_c y'_b, z'_b)}, \tag{6c}$$

with $H' = \left|\boldsymbol{H}'(x', y', z', L_c, W_m, H_m, Y_m, Y_c)\right|$ and

$$\beta == \frac{y_m^7}{24\pi^2 \ell_m^3 w_m^2 h_m^2} \quad \frac{Y_m^7}{24\pi^2 W_m^2 H_m^2}. \tag{7}$$

Typically Y_c is small (for our experiments $Y_c = 0.05$) so we may exploit this small parameter by considering the system (6) at leading order in Y_c, subject to the initial conditions $(x'_b(0), y'_b(0), z'_b(0)) = (0, 0, 0)$. This provides the bead trajectory

$$x'_b(t') = t', \tag{8a}$$

$$y'_b(t') = \Omega\beta \int_0^{t'} \frac{\partial H'(\tilde{t}, 0, 0, L_c, W_c, H_c, Y_m, 0)^2}{\partial y'} d\tilde{t}, \tag{8b}$$

$$z'_b(t') = 0. \tag{8c}$$

(We note that $\partial H'^2 / \partial z' \equiv 0$ on $z' = 0$ so that the right-hand side of (6c) is identically zero to all orders in Y_c.) Hence the dimensionless magnetic bead exit position scaled with y_c is given by $y'_e = y'_b(L_c) = \kappa\Omega$ where

$$\kappa = \beta \int_0^{L_c} \frac{\partial H'(\tilde{t}, 0, 0, L_c, W_c, H_c, Y_m, 0)^2}{\partial y'} d\tilde{t}. \tag{9}$$

The detailed calculation has allowed us to determine an explicit expression for the coefficient κ, in terms of the geometrical properties of the system. For the system we study, we calculate $\kappa \approx 0.01$.

We plot in Figure 4 the dimensionless exit position y'_e against the design parameter *Ω*. The solid line indicates the relationship predicted by our model, with the slope $\kappa \approx 0.01$ predicted by the detailed calculation. Note that in the experiments we have varied bead radius (a) and susceptibility (χ), the magnet stack length (ℓ_m), average fluid velocity (u_o), and the normal distance between the magnet and the channel, (y_m). By comparing the experimental data with our theory we find the magnetic susceptibilities of the 0.5 μm and 1.4 μm radii beads, respectively, χ = 2.5 x 10^{-2} (+/- 5 x 10^{-3}) and 2 x 10^{-2} (+/- 3 x 10^{-3}). The magnetic susceptibilities of the beads vary between batches during the manufacturing process and the values we obtain are within a factor of 10 of those reported in the literature.[18, 27] (They also vary by up to a factor of 10.) We find that the data collapses onto the theoretical curve, $y'_e = \kappa\Omega$.

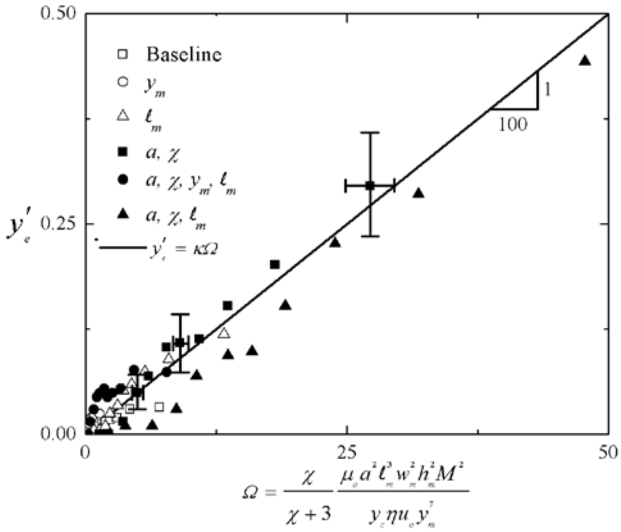

Figure 4 Dimensionless exit position y'_e plotted versus the dimensionless design parameter *Ω*. The theoretical model equation, $y'_e = \kappa\Omega$, is plotted with a solid line, where $\kappa \approx 0.01$. The data for the exit position collapses onto the theoretical curve.

Conclusions

In this paper, we present experiments that show the variables that control the exit positions of paramagnetic beads in a microfluidic magnetic multi-target sorter. The important variables we find are: bead size and susceptibility, magnet size and magnetization, fluid speed and viscosity, and channel geometry. We present a model that predicts the exit position of the paramagnetic beads, and is in good agreement with our experimental measurements.

In the future, microfluidic immunomagnetic multi-target sorting, such as sorting different cells, can be accomplished by incubating the cells with a suspension of paramagnetic beads of different sizes and susceptibilities. The cells that present antigen specific to antibodies coated on particular beads will bind to those beads. Flowing the solution through the microfluidic immunomagnetic multi-target sorter we present here will result in the different cells exiting at different positions in the channel. The dimensionless design parameter, *Ω*, we describe in this paper will be useful for future designers of microfluidic immunomagnetic multi-target sorters in choosing beads, magnets, flow rate, as well as geometry.

Appendix

In this section, we calculate the magnetic field generated by a three-dimensional, rectangular magnet of dimensions ℓ_m x w_m x h_m and magnetized in the *x*-direction as shown in Figure 1(c). The magnetic vector potential, $\boldsymbol{A}$, is given by

$$\boldsymbol{A} = \frac{\mu_o}{4\pi}\iiint \frac{\boldsymbol{M}\times\hat{\boldsymbol{r}}}{r^2}\,dV \quad \frac{\mu_o M \ell_m}{4\pi}\boldsymbol{A}', \tag{10}$$

where

$$\boldsymbol{A}' = \int_{-\frac{H_m}{2}}^{\frac{H_m}{2}} \int_{Y_m-\frac{W_m}{2}}^{Y_m+\frac{W_m}{2}} \int_{\frac{L_c-1}{2}}^{\frac{L_c+1}{2}} \frac{\hat{\boldsymbol{x}}\times\hat{\boldsymbol{r}}}{\left(\tilde{x}-x'\right)^2+\left(\tilde{y}-y'\right)^2+\left(\tilde{z}-z'\right)^2}\,d\tilde{x}d\tilde{y}d\tilde{z}, \tag{11}$$

$\hat{\boldsymbol{r}} = \boldsymbol{r}/|\boldsymbol{r}|$, $\boldsymbol{r} = \left(\tilde{x}-x', \tilde{y}-y', \tilde{z}-z'\right)$, $\hat{\boldsymbol{x}}$ represents the unit vector in the *x*-direction, and we have non-dimensionalized as in (4) and (5).

The integral (10) may be evaluated analytically, though the result is lengthy so we do not write it down here. Once determined, the magnetic field, $\boldsymbol{H}'\left(x', y', z', L_c, W_m, H_m, Y_m, Y_c\right)$ is then given by the relation

$$\mu_o \boldsymbol{H} = \nabla\times\boldsymbol{A}, \tag{12}$$

Which provides an explicit expression for the dimensionless magnetic field, $\boldsymbol{H}'$, non-dimensionalized as in (6).

Acknowledgements

We are grateful to the National Science Foundation **(Grant# and NSF#)** for providing funding for our research. We also thank J. Wan and M. C. McAlpine for helpful discussions and C.W. Yung for early inspirations of this project.

Notes

[a] *School of Engineering and Applied Sciences, Harvard University, Cambridge, MA, 02138, USA; E-mail: stsai@seas.harvard.edu*
[b] *Mathematical Institute, University of Oxford, Oxford, 0X1 3LB, England; E-mail: ian.griffiths@maths.ox.ac.uk*
[c] *Department of Mechanical and Aerospace Engineering, Princeton University, Princeton, NJ, 08544, USA; E-mail: hastone@princeton.edu*

† Electronic Supplementary Information (ESI) available: [details of any supplementary information available should be included here]. See DOI: 10.1039/b000000x/

References

1. S. Miltenyi, W. Muller, W. Weichel and A. Radbruch, *Cytometry*, 1990, **11**, 231-238.
2. A. S. Brodsky and P. A. Silver, *Mol. Cell. Proteomics*, 2002, **1**, 922-929.

3. Q. Meng, C. Wong, A. Rangachari, S. Tamatsukuri, M. Sasaki, E. Fiss, L. Cheng, T. Ramankutty, D. Clarke, H. Yawata, Y. Sakakura, T. Hirose and C. Impraim, *J. Clin. Microbiol.*, 2001, **39**, 2937-2945.
4. D. W. Inglis, R. Riehn, R. H. Austin and J. C. Sturm, *Appl. Phys. Lett.*, 2004, **85**, 5093-5095.
5. D. W. Inglis, R. Riehn, J. C. Sturm and R. H. Austin, *J. Appl. Phys.*, 2006, **99**.
6. C. W. Yung, J. Fiering, A. J. Mueller and D. E. Ingber, *Lab Chip*, 2009, **9**, 1171-1177.
7. L. Saias, A. E. Saliba, J. L. Viovy, J. Y. Pierga, P. Vielh and F. Farace, *Houille Blanche-Revue Internationale De L Eau*, 2009, 105-111.
8. A. E. Saliba, L. Saias, J. Salamero, V. Fraisier, J. Y. Pierga, F. C. Bidard, C. Mathiot, P. Vielh, F. Farace and J. L. Viovy, *Anticancer Res.*, 2008, **28**, 3530-3531.
9. A. Sinha, R. Ganguly, A. K. De and I. K. Puri, *Phys. Fluids*, 2007, **19**, 117102.
10. C. Mikkelsen and H. Bruus, *Lab Chip*, 2005, **5**, 1293-1297.
11. C. Mikkelsen, M. F. Hansen and H. Bruus, *J. Magn. Magn. Mater.*, 2005, **293**, 578-583.
12. E. P. Furlani, *J. Appl. Phys.*, 2006, **99**.
13. S. S. Shevkoplyas, A. C. Siegel, R. M. Westervelt, M. G. Prentiss and G. M. Whitesides, *Lab Chip*, 2007, **7**, 1294-1302.
14. N. Modak, A. Datta and R. Ganguly, *Microfluidics and Nanofluidics*, 2009, **6**, 647-660.
15. K. Nandy, S. Chaudhuri, R. Ganguly and I. K. Puri, *J. Magn. Magn. Mater.*, 2008, **320**, 1398-1405.
16. B. Le Drogoff, L. Clime and T. Veres, *Microfluidics and Nanofluidics*, 2008, **5**, 373-381.
17. T. Baier, S. Mohanty, K. S. Drese, F. Rampf, J. Kim and F. Schonfeld, *Microfluidics and Nanofluidics*, 2009, **7**, 205-216.
18. N. Pamme and A. Manz, *Anal. Chem.*, 2004, **76**, 7250-7256.
19. N. Pamme, J. C. T. Eijkel and A. Manz, *J. Magn. Magn. Mater.*, 2006, **307**, 237-244.
20. C. Carr, M. Espy, P. Nath, S. L. Martin, M. D. Ward and J. Martin, *J. Magn. Magn. Mater.*, 2009, **321**, 1440-1445.
21. J. D. Adams, U. Kim and H. T. Soh, *Proc. Natl. Acad. Sci. U. S. A.*, 2008, **105**, 18165-18170.
22. C. X. Liu, L. Lagae, R. Wirix-Speetjens and G. Borghs, *J. Appl. Phys.*, 2007, **101**, -.
23. A. Weddemann, F. Wittbracht, A. Auge and A. Hutten, *Appl. Phys. Lett.*, 2009, **94**, -.
24. N. Pamme and C. Wilhelm, *Lab Chip*, 2006, **6**, 974-980.
25. J. R. Anderson, D. T. Chiu, R. J. Jackman, O. Cherniavskaya, J. C. McDonald, H. K. Wu, S. H. Whitesides and G. M. Whitesides, *Anal. Chem.*, 2000, **72**, 3158-3164.
26. J. B. Knight, A. Vishwanath, J. P. Brody and R. H. Austin, *Phys. Rev. Lett.*, 1998, **80**, 3863-3866.
27. G. Fonnum, C. Johansson, A. Molteberg, S. Morup and E. Aksnes, *J. Magn. Magn. Mater.*, 2005, **293**, 41-47.

RECENT REPORTS

12/78	A Review of Mathematical Models for the Formation of Vascular Networks	Scianna Bell Preziosi
12/79	Fast and Accurate Computation of Gauss-Legendre and Gauss-Jacobi Quadrature Nodes and Weights	Hale Townsend
12/80	On the spectral distribution of kernel matrices related to radial basis functions	Wathen Zhu
12/81	Inner product computation for sparse iterative solvers on distributed supercomputer	Zhu Gu Liu
12/82	A new pathway for the re-equilibration of micellar surfactant solutions	Griffiths Breward Colegate Dellar Howell Bain
12/83	Object-Oriented Paradigms for Modelling Vascular Tumour Growth: a Case Study	Connor Cooper Byrne Maini McKeever
12/84	Chaste: an open source C++ library for computational physiology and biology	Mirams Arthurs Bernabeu Bordas Cooper Corrias Davit Dunn Fletcher Harvey Marsh Osborne Pathmanathan Pitt-Francis Southern Zemzemi Gavaghan
12/85	A two-pressure model for slightly compressible single phase flow in bi-structured porous media	Schlackow Marguerat Proudfoot Bähler Erban Gullerova
12/86	Boolean modelling reveals new regulatory connections between transcription factors orchestrating the development of the ventral spinal cord	Lovrics Gao Juhász Bock Byrne

12/91	Biaxial defect cores in nematic equilibria: an asymptotic result	Majumdar Pisante Henao
12/92	The Three Sphere Swimmer in a Nonlinear Viscoelastic Medium	Curtis Gaffney
12/93	Diffusion of multiple species with excluded-volume effects	Bruna Chapman
12/94	The Mechanics of a Chain or Ring of Spherical Magnets	Hall Vella Goriely
12/95	On-Lattice Agent-based Simulation of Populations of Cells within the Open-Source Chaste Framework	Figueredo Joshi Osborne Byrne Owen
12/96	Mathematical Biomedicine and Modeling Avascular Tumor Growth	Byrne
12/97	Inference of the genetic network regulating lateral root initiation in Arabidopsis thaliana	Muraro Voß Wilson Bennett Byrne De Smet Hodgman King
12/98	Axisymmetric bifurcations of thick spherical shells under inflation and compression	deBotton Bustamante Dorfmann
12/99	Calculus from the past: Multiple Delay Systems arising in Cancer Cell Modelling	Wake Byrne
12/100	Nonlocal models of electrical propagation in cardiac tissue: electrotonic effects and the modulated dispersion of repolarization	Bueno-Orovio Kay Grau Rodriguez Burrage

Copies of these, and any other OCCAM reports can be obtained from:

Oxford Centre for Collaborative Applied Mathematics
Mathematical Institute

24 - 29 St Giles'
Oxford
OX1 3LB
England
www.maths.ox.ac.uk/occam